RESEARCH ARTICLE

QUANTUM CRITICALITY

Tunable quantum criticality and super-ballistic transport in a "charge" Kondo circuit

Z. Iftikhar[1], A. Anthore[1,2], A. K. Mitchell[3], F. D. Parmentier[1]*, U. Gennser[1], A. Ouerghi[1], A. Cavanna[1], C. Mora[4], P. Simon[5], F. Pierre[1]†

Quantum phase transitions (QPTs) are ubiquitous in strongly correlated materials. However, the microscopic complexity of these systems impedes the quantitative understanding of QPTs. We observed and thoroughly analyzed the rich strongly correlated physics in two profoundly dissimilar regimes of quantum criticality. With a circuit implementing a quantum simulator for the three-channel Kondo model, we reveal the universal scalings toward different low-temperature fixed points and along the multiple crossovers from quantum criticality. An unanticipated violation of the maximum conductance for ballistic free electrons is uncovered. The present charge pseudospin implementation of a Kondo impurity opens access to a broad variety of strongly correlated phenomena.

Continuous second-order quantum phase transitions (QPTs)—which take place at absolute zero temperature as a control parameter such as the magnetic field is tuned—are accompanied by the development of a highly correlated quantum critical state. With increasing temperature, this state extends over a broadening range of parameters further away from the critical point. In this regime of quantum criticality, the properties of the system obey scaling laws determined by the QPT universality class and do not depend on microscopic details. Although QPTs are ubiquitous in contemporary theoretical physics and have been observed in a multitude of highly correlated materials (*1*), it remains challenging to realize them in simple, well-controlled experimental systems.

Tunable nanostructures provide a path to a microscopic understanding of QPTs that circumvents the complexity of real-world highly correlated materials. So far, however, the rare examples that exhibit a second-order QPT (*2*–*6*) demonstrate only a single quantum critical point (associated with the two-channel Kondo effect, described below); although it is a non-Fermi liquid, this critical point can be treated with a perturbative approach in the low-temperature limit (*7*, *8*). By contrast, we realized and characterized completely a circuit that embodies the three-channel Kondo model, with three fully tunable channels connected to a magnetic impurity emulated by the charge states of a metallic island. Within the same nanostructure, this gives us access to two universality classes of quantum criticality (associated with the two-channel and three-channel Kondo effects) that manifest profoundly dissimilar physics. For instance, the quantum critical point for two symmetric Kondo channels can be understood in terms of free electrons and Majorana fermions (*7*, *8*), whereas for three symmetric channels, it involves ($\mathbb{Z}_3$) parafermions with irreducibly strong interactions (*9*). The demonstrated high-precision implementation qualifies our device as an analog quantum simulator, providing quantitative experimental solutions for the three-channel Kondo model.

The multichannel Kondo model

The multichannel Kondo model, which is a generalization of the original (one channel) Kondo model, gives rise to archetypal QPTs and collective, non-Fermi liquid behaviors from a minimal Hamiltonian. Although introduced to account for the different atomic orbitals in metals (*10*–*12*), it has developed over the years into a central testing ground for strongly correlated and quantum critical physics and is a benchmark for many-body theoretical methods (*7*, *11*–*19*). The model describes a local Kondo spin S (of 1/2 here) coupled antiferromagnetically to N independent free-electron continua (Fig. 1A, $N = 3$)

$$H_{\mathrm{NCK}} = \sum_{i=1}^{N} J_i \mathbf{s_i} \cdot \mathbf{S} + H_{\mathrm{continua}} \qquad (1)$$

where H_{NCK} is the N-channel Kondo Hamiltonian, $\mathbf{s_i}$ is the local spin density of electron continuum (channel) i at the Kondo spin $\mathbf{S}$ location, $J_i > 0$ is the coupling strengths (here assumed isotropic), and H_{continua} is the free-electron continua Hamiltonian. The conventional single-channel model ($N = 1$) exhibits universal scaling but no second-order QPT or non-Fermi liquid physics. As the temperature T is reduced, the electrons progressively screen the Kondo spin, resulting for $T \to 0$ in an idle spin-singlet (*11*). By contrast, for $N \geq 2$, there is a competition between channels to screen the $S = 1/2$ Kondo impurity, which develops into second-order QPTs. Each number of identical channels corresponds to a different class of quantum criticality (*16*), with specific non-Fermi liquid physics (*12*) and collective excitations revealed by, for example, a divergent specific heat coefficient c/T as $T \to 0$. The marginal two-channel case corresponds to a logarithmic c/T divergence (*12*), whereas power law c/T divergences are predicted for $N \geq 3$ (*12*).

Kondo "charge" pseudospin implementation

Experimentally, Kondo nanostructures are usually small quantum dots (*20*–*23*), in which coherent electron cotunneling merges the distinct electrical contacts into one Kondo channel (*24*, *25*) [except in the two-channel devices in (*2*, *5*, *26*, *27*)]. By contrast, in the recently demonstrated (*6*) "charge" Kondo approach (*14*, *28*, *29*), the charge Kondo impurity $\mathbf{S}$ is not a magnetic spin but a pseudospin-1/2 (Fig. 1B, red arrow) built from the macroscopic quantum states describing the overall charge Q of a small metallic island (Fig. 1B, red disk). We extended this concept to three independent Kondo channels. In the most straightforward case of a weakly connected island whose charge is well quantized (*30*), the Kondo spin $S = \{\downarrow, \uparrow\}$ directly maps on the island's two charge states of lowest energy $\{Q, Q + e\}$. All the other charge configurations are indeed frozen out and can be ignored at low temperatures $T \ll E_{\mathrm{C}}/k_{\mathrm{B}}$ ($E_{\mathrm{C}} = e^2/2C$ is the charging energy, e is the electron charge, C is the island geometric capacitance, and k_{B} is the Boltzmann constant). The charge pseudospin energy degeneracy is obtained by tuning (with a gate voltage V_{g}) the device at the degeneracy point between the charge states Q and $Q + e$. Detuning V_{g} away from charge degeneracy is completely analogous to applying a magnetic field on usual magnetic Kondo impurities (*28*). The island charge Kondo pseudospin S is, however, not coupled to the real spin of electrons. Instead, it is flipped by transferring electrons in and out of the island, through the connected electrical channels (Fig. 1B, red dashed lines). This mechanism takes the form of a Kondo (pseudo-) spin-exchange coupling: Introducing an electron pseudospin s (Fig. 1B, blue arrow), which corresponds to the electron localization inside ($s = \downarrow$) or outside ($s = \uparrow$) of the island, the tunneling of an electron flips both its localization pseudospin s as well as the island overall charge pseudospin S. A well-developed Kondo effect requires a continuum of electronic states

[1]Centre de Nanosciences et de Nanotechnologies (C2N), CNRS, Univ. Paris-Sud, Université Paris-Saclay, 91120 Palaiseau, France. [2]Univ. Paris Diderot, Sorbonne Paris Cité, 75013 Paris, France. [3]School of Physics, University College Dublin, Dublin 4, Ireland. [4]Laboratoire Pierre Aigrain, Ecole Normale Supérieure–PSL Research University, CNRS, UPMC Univ. Paris 06–Sorbonne Universités, Univ. Paris Diderot-Sorbonne Paris Cité, 75005 Paris, France. [5]Laboratoire de Physique des Solides, CNRS, Univ. Paris-Sud, Université Paris-Saclay, 91405 Orsay, France.
*Present address: Service de Physique de l'État Condensé, CEA, CNRS, Université Paris Saclay, CEA-Saclay 91191 Gif-sur-Yvette, France.
†Corresponding author. Email: frederic.pierre@u-psud.fr

Downloaded from http://science.sciencemag.org/ on September 20, 2019

for both localization pseudospins. This implies a continuous density of states in the metallic island (in contrast with small quantum dots). The different conduction channels constitute here separate Kondo channels. Also, the same physics is predicted at $T \ll E_C/k_B$ for arbitrary connection strengths (*14*, *31*, *32*), except perfectly ballistic contacts, despite the coexistence of many charge states in a quantum superposition near the ballistic limit (*30*). In practice, we found from numerical renormalization group (NRG) calculations performed over a broad range of coupling strengths that $T \lesssim E_C/20k_B$ ensures negligible deviations from universal Kondo physics (*32*).

Each of the Kondo/conduction channels passes through a different quantum point contact (QPC) individually formed and tuned by means of field effect in a high-mobility Ga(Al)As two-dimensional electron gas (*32*). Single channels, polarized in real electron spin, are obtained by immersing the device into a large magnetic field ($B \simeq 2.7$ T, corresponding to the regime of the integer quantum Hall effect at filling factor $\nu = 3$). The Kondo channel couplings J_i ($i \in \{1, 2, 3\}$) are individually characterized by the "intrinsic" (unrenormalized by Kondo or Coulomb effects) transmission probability τ_i across the single open transport channel of QPC$_i$. The micrometer-scale separation between QPCs enables independent fine tuning (~0.1%) and high-precision characterization [$\lesssim$2%, with a large dc bias voltage suppressing Kondo/Coulomb renormalization (*32*)] of the Kondo channels, over the full range $\tau_i \in [0, 1]$. Such fine tuning of the connected channels to identical couplings is crucial for approaching the frustrated, symmetric Kondo critical points. The two-channel Kondo (2CK) configurations are implemented by setting $\tau_1 \simeq \tau_3 \equiv \tau$ and $\tau_2 = 0$, whereas for the three-channel Kondo (3CK) configurations $\tau_1 \simeq \tau_2 \simeq \tau_3 \equiv \tau$. With the charging energy $E_C \simeq k_B \times 0.3$ K (separately obtained from Coulomb diamond measurements) and high-precision shot-noise thermometry (*33*), the device is completely characterized. The knowledge of these parameters allows for a full quantitative microscopic understanding (*19*, *28*, *29*). In practice, Kondo physics is observed through the renormalized QPC conductances G_i measured in situ. Because the symmetry between channels is found preserved by renormalization (at an experimental accuracy of ~$0.003e^2/h$), we generally display the averages $G_{1,3} \equiv (G_1 + G_3)/2$ and $G_{1,2,3} \equiv (G_1 + G_2 + G_3)/3$ when investigating the symmetric 2CK and 3CK configurations, respectively.

The high-precision implementation/quantum simulation of the charge Kondo model is validated in Fig. 1, C and D, and the different two-channel and three-channel Kondo behaviors are qualitatively illustrated. The renormalized conductance across channels tuned to "intrinsic" $\tau \simeq 0.90$ (Fig. 1, C and D, squares) or 0.68 (Fig. 1, C and D, triangles) is displayed for $T \simeq 7.9$ and 29 mK while sweeping the gate voltage V_g. The charge degeneracy point is identified as the conductance peak ($\delta V_g = 0$). The good match, without any fit parameters, between the conductance data and the quantitative predictions of the charge Kondo model derived analytically for two near ballistic channels at low temperature (Fig. 1C, continuous line) (*29*, *32*) attests to the accurate device characterization and to its precise implementation of the model for arbitrary Kondo pseudospin energy splitting (*19*, *32*). At large δV_g, the conductance is systematically reduced upon lowering T as usually expected from plain charge quantization. At $\delta V_g = 0$ and for two or three symmetric channels set to $\tau \simeq 0.68$, we observed instead a conductance increase with T owing to the Kondo renormalization of weakly connected channels. At the larger $\tau \simeq 0.90$, 2CK and 3CK exhibit qualitatively different conductance renormalizations at $\delta V_g = 0$, with opposite signs.

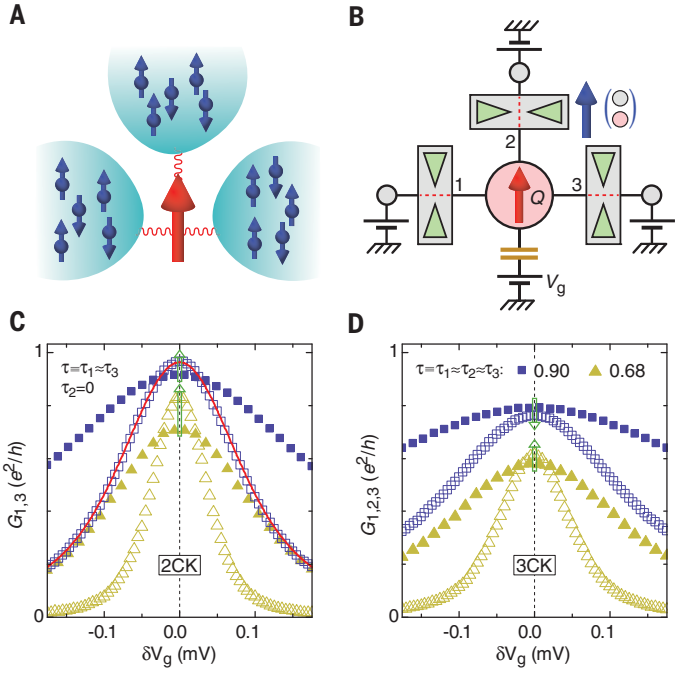

Fig. 1. Multichannel Kondo model and charge implementation. (**A**) In the Kondo model, a local spin (red arrow) is antiferromagnetically coupled to the spin of electrons (blue arrows). Each Kondo channel corresponds to one distinct electron continuum (three continua are shown here). (**B**) Sample schematic realizing the charge pseudospin implementation of the three-channel Kondo model. A micrometer-scale metallic island (red disk) is connected to large electrodes (small gray disks) through three QPCs (green split gates), each set to a single (spin-polarized) conduction channel (red dashed lines) indexed by $i \in \{1, 2, 3\}$. (**C** and **D**) Quantum channels conductance measured versus gate voltage V_g is displayed over half a Coulomb oscillation period $\Delta \simeq 0.7$ mV (several sweeps including different consecutive peaks are averaged). Measurements at $T \simeq 7.9$ and 29 mK are shown, respectively, as open and full symbols for two (C) or three (D) symmetric channels. The squares correspond to an "intrinsic," unrenormalized transmission probability across the connected QPCs of $\tau \simeq 0.90$, and triangles to that of $\tau \simeq 0.68$. The red continuous line (C) displays the $T = 7.9$ mK prediction for two channels both set to $\tau = 0.90$ (*32*). Green arrows indicate the direction of conductance change at $\delta V_g = 0$ as temperature is reduced.

Observation of an intermediate nontrivial fixed point

The above findings corroborate the theoretical expectations for the different 2CK and 3CK low-temperature conductance fixed points (*29*, *34*). Both 2CK and 3CK quantum critical fixed points are associated with an intermediate value of the renormalized Kondo coupling $0 < |J| < \infty$ (*10*, *12*). In previous experiments on small quantum dots (*2*, *5*), the 2CK intermediate coupling could not be established. Indeed, T was not low enough with respect to the scaling Kondo temperature T_K to show a saturation; furthermore, asymmetries between electrical channels (*15*) can lead to a trivial intermediate asymptotic value of the measured conductance, which therefore does not necessarily imply an intermediate coupling in these spin Kondo devices. Moreover, the intermediate coupling character of the 2CK fixed point is not entirely invariable but depends on the choice of representation (*7*, *8*, *14*, *29*). In particular, the 2CK fixed point can be described as a noninteracting system involving two Majorana modes [one free, one in the strong coupling limit (*7*)]. This dual strong-coupling character of the 2CK fixed point also materializes in the present charge Kondo implementation: Here, $G_{1,3}$ constitutes an alternative probe of the coupling between electrons and charge Kondo impurity, which flows not toward an intermediate value per electrical channel but toward the maximum free-electron quantum limit $G_{2CK} = e^2/h$ (*29*). By contrast, the genuinely intermediate character of the interacting 3CK fixed point is predicted to show up directly in charge Kondo circuits, as a flow of the conductance per channel $G_{1,2,3}$ toward the nontrivial intermediate universal conductance $G_{3CK} = 2\sin^2(\pi/5)e^2/h \simeq 0.691e^2/h$ (*34*).

The precise 2CK and 3CK low-temperature universal conductance fixed points are experimentally established by measuring the temperature evolution of $G_{1,3}$ and $G_{1,2,3}$, respectively, for a broad range of symmetric channel settings [$\tau \in (0.56, 0.985)$]. For this purpose, and until explicitly specified otherwise, the device is tuned

Downloaded from http://science.sciencemag.org/ on September 20, 2019

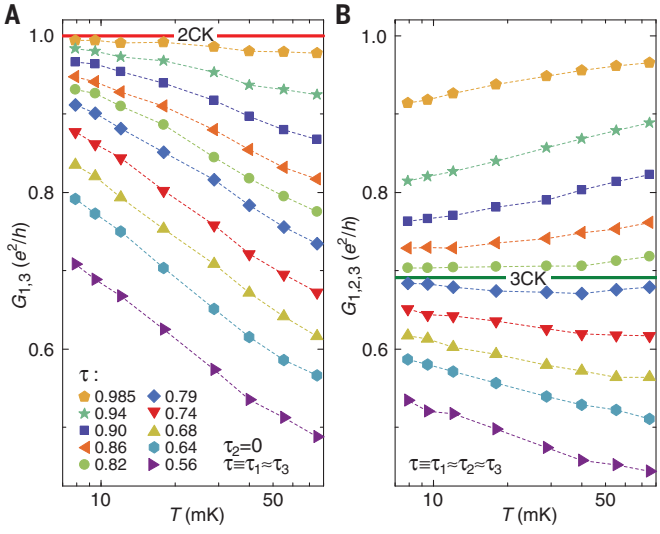

Fig. 2. Quantum critical fixed points. (**A** and **B**) The conductance of (A) two or (B) three symmetric channels measured at the charge degeneracy point ($\delta V_g = 0$) is plotted as symbols versus temperature on a logarithmic scale. Each set of identical symbols connected by dashed lines corresponds to the same device setting (τ). The predicted (A) 2CK and (B) 3CK low-temperature fixed points for the conductance per channel in the present charge Kondo implementation are shown as horizontal continuous lines [$G_{2CK} = e^2/h$, $G_{3CK} = 2\sin^2(\pi/5)e^2/h$].

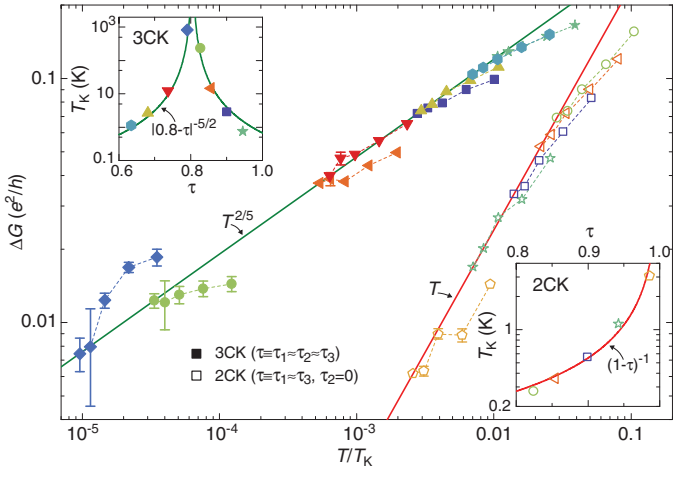

Fig. 3. Non-Fermi liquid scaling exponents. The absolute difference between symmetric channels conductance at charge degeneracy and predicted Kondo fixed point ($\Delta G \equiv |G_{1,3} - G_{2CK}|$ and $\Delta G \equiv |G_{1,2,3} - G_{3CK}|$) is plotted as symbols (open and solid for 2CK and 3CK, respectively) versus T/T_K in a log-log scale for $T \in \{7.9, 9.5, 12, 18, 29\}$ mK. Statistical error bars are shown when larger than symbols. The red and green continuous straight lines display the predicted power-law scaling at $T/T_K \ll 1$ for the conductance per channel in the present charge 2CK and 3CK implementations, respectively. The scaling Kondo temperature T_K is adjusted separately for each tuning τ of the symmetric channels (insets, corresponding symbols). This is done by matching the lowest-temperature data point $\Delta G(T \simeq 7.9$ mk) with the corresponding displayed power law. Continuous lines in insets show the predicted power-law divergences of T_K versus τ for 2CK (bottom right inset) and 3CK (top left inset).

at charge degeneracy ($\delta V_g = 0$), where Kondo effect is expected. Measurements of $G_{1,3}$ and $G_{1,2,3}$ versus T in logarithmic scale are shown as symbols in Fig. 2. In the 2CK configuration (Fig. 2A), whatever the setting τ, we found that $G_{1,3}$ always grows as T is reduced. This observation validates the predicted e^2/h Kondo fixed point (Fig. 2A, horizontal red line), at an experimental accuracy of $0.006e^2/h$ (*6*). Upon lowering T in the 3CK configuration (Fig. 2B), $G_{1,2,3}$ systematically grows when below $0.68e^2/h$ (and for $T \leq 40$ mK) and decreases when above $0.70e^2/h$. This validates the predicted 3CK universal conductance fixed point $G_{3CK} \simeq 0.69e^2/h$ (horizontal green line) at an experimental accuracy of $\pm 0.01e^2/h$. This constitutes direct experimental evidence of an intermediate non-Fermi liquid fixed point.

Universal scalings toward quantum criticality

First, we characterized the power-law exponents when approaching the 2CK and 3CK low-temperature fixed points and found them to be different from the characteristic T^2 for Fermi liquids. For this purpose, the distances ΔG between measured $G_{1,3}$ and $G_{1,2,3}$ and, respectively, the theoretically predicted fixed points G_{2CK} and G_{3CK} are plotted in Fig. 3 versus T/T_K. The continuous straight lines show the universal power-law scalings asymptotically predicted at low T/T_K for the conductance in the present charge Kondo implementation: $\Delta G \propto T$ for 2CK (*19*, *29*, *35*) and $\Delta G \propto T^{2/5}$ for 3CK (*12*, *13*, *32*) [further discussion is provided in (*32*)]. Comparing with the data requires us to, for each τ, fix the corresponding scaling Kondo temperature $T_K(\tau)$. Symbols in the Fig. 3 insets represent the experimentally extracted values of T_K versus τ, which were obtained for each tuning τ by matching the lowest-temperature data point with the displayed theoretical power law. The data-theory comparison in the main Fig. 3 panel is therefore in the conductance evolution as temperature is increased. We found that sufficiently close to the fixed points ($\Delta G \lesssim 0.1e^2/h$), the experiment is consistent with predictions. The precision is here limited by the increasing relative experimental uncertainty as ΔG is reduced. A direct extraction of the temperature exponents from the $\Delta G < 0.1e^2/h$ data at $T \in \{7.9, 12\}$ mK (satisfying the NRG universality criteria $T \lesssim E_C/20k_B \simeq 15$ mK) gives $\alpha_{2CK} = 0.83 \pm 0.08$ for 2CK and $\alpha_{3CK} = 0.42 \pm 0.17$ for 3CK.

We then investigated the full 2CK and 3CK universal renormalization flows. Measurements (symbols) are now compared in Fig. 4, A to C, with NRG calculations spanning the whole range of T/T_K (Fig. 4, continuous black lines) (*32*). In Fig. 4, A and B, respectively, $G_{1,3}$ and $G_{1,2,3}$ are plotted versus $\log(T/T_K)$. Following standard procedures, the theoretical scaling Kondo temperature T_K was normalized so that the NRG universal conductance takes a value equal to half that of the Kondo fixed point at $T = T_K$. As in Fig. 3, the experimental $T_K(\tau)$ (symbols in Fig. 4 insets) are adjusted by matching data with theory at $T \simeq 7.9$ mK. These $T_K(\tau)$ remain therefore identical to those in the insets of Fig. 3 as long as NRG calculations and asymptotic power laws are indistinguishable (for $T_K \gg 7.9$ mK). We observed a quantitative agreement between the data and the universal NRG prediction over six (2CK) or eight (3CK) orders of magnitude in T/T_K. A direct comparison of the same measurements and predictions is shown in Fig. 4C in a scale-invariant representation that does not involve rescaling the temperature in units of T_K, by displaying $\partial G_{1,3}/\partial \log(T)$ versus $G_{1,3}$ and $\partial G_{1,2,3}/\partial \log(T)$ versus $G_{1,2,3}$. In this representation, data points correspond to experimental measurements of the so-called β-function that determines the corresponding 2CK or 3CK renormalization group equation for the conductance. In Fig. 4C, the straight dashed lines near 2CK and 3CK fixed points (Fig. 4C, arrows) represent the predicted non-Fermi liquid power-law behaviors discussed in the previous paragraph. Comparing with the experimental slope therefore complements the approach in Fig. 3. Also shown is the experimental "analog quantum simulation" of the universal 3CK β-function at $G_{1,2,3} > G_{3CK}$, out of reach of NRG calculations.

Last, we explored the quantitative relationship between scaling Kondo temperature T_K and microscopic model parameter τ (Figs. 3 and 4, insets). At small $\tau \lesssim 0.5$, the same expected exponential behavior $T_K \simeq (E_C/10k_B)\exp(-\pi^2/\sqrt{4\tau})$ is observed for 2CK and 3CK (*29*). At larger τ, T_K appears to diverge at a specific setting τ_c, with extracted T_K values orders of magnitude above

Downloaded from http://science.sciencemag.org/ on September 20, 2019

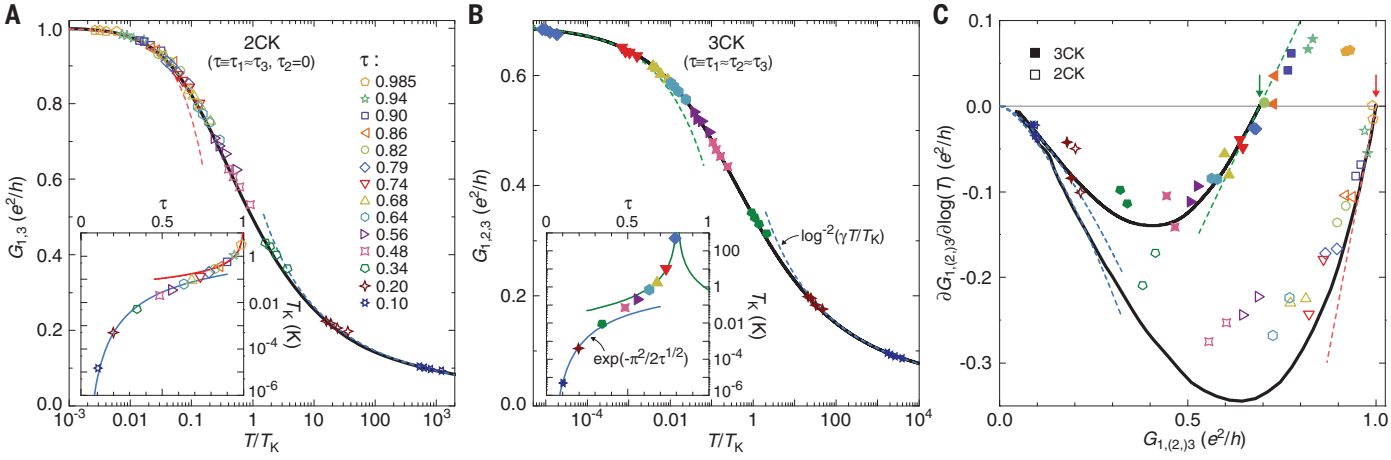

Fig. 4. Universal renormalization flow to quantum criticality. The measured conductance of the two or three connected, symmetric channels is shown as symbols (open and solid for 2CK and 3CK, respectively) for a broad range of settings τ. (**A** and **B**) Data ($T \in \{7.9, 9.5, 12, 18\}$ mK) and predictions are plotted versus T/T_K in log scale. The corresponding experimental T_K are shown in insets as symbols versus τ, together with theoretical predictions for tunnel contacts $\tau \ll 1$ (light-blue continuous lines) and for very large T_K at $|\tau - \tau_c| \ll 1$ [respectively, red and green continuous lines for 2CK and 3CK in insets of (A) and (B)]. (**C**) Direct data-theory comparison (no T/T_K rescaling) with $\partial G_{1,3}/\partial \log(T)$ plotted versus $G_{1,3}$ and $\partial G_{1,2,3}/\partial \log(T)$ plotted versus $G_{1,2,3}$. The discrete experimental differentiation is performed with measurements at $T \in \{7.9, 12, 18\}$ mK. Kondo fixed points are indicated by arrows. Black continuous lines are NRG calculations of the universal renormalization flows [2CK in (A) and (C) and 3CK in (B) and (C)]. Colorized dashed lines shown at low T/T_K [(A) and (B)], and close to the Kondo fixed points (C), display the predicted low-temperature power laws for 2CK [red in (A) and (C)] and 3CK [green in (B) and (C)]. Light blue dashed lines shown at large T/T_K [(A) and (B)], and for small channels conductance (C), represent the predicted high-temperature logarithmic scaling proportional to $\log^{-2}(\gamma T/T_K \gg 1)$, with the slightly different 2CK and 3CK prefactors and γ here used as fit parameters.

the high-energy cutoff $E_C/k_B \simeq 300$ mK (in which case, universal Kondo physics can only be probed at $T/T_K \ll 1$). For 2CK, theory predicts a divergence at $\tau_c = 1$ as $T_K(1-\tau \ll 1) \propto 1/(1-\tau)$, which is displayed by the identical continuous red lines in the insets of Figs. 3 and 4A (*29*) [(*31*, *36*), the prediction of a peaked $T_K(J)$]. For 3CK, the observed value $\tau_c \simeq 0.8$ is higher than $G_{3CK}h/e^2 \simeq 0.69$. This is caused by the conductance suppression by Coulomb interaction at temperatures $T \gtrsim E_C/k_B$, before the development of universal Kondo physics at low temperatures. Assuming theoretically that T_K diverges at τ_c, we generally find (*32*) that a low-temperature conductance power law $\Delta G \propto T^\alpha$ corresponds to a power-law divergence as $T_K \propto |\tau - \tau_c|^{-1/\alpha}$. The observed close agreement between experimental $T_K(|\tau - \tau_c| \ll 1)$ in 2CK and 3CK configurations with, respectively, $T_K \propto |\tau - 1|^{-1}$ (Figs. 3 and 4A, insets, red lines) and $T_K \propto |\tau - 0.8|^{-5/2}$ (Figs. 3 and 4B, insets, green lines) therefore further establishes the predicted non-Fermi liquid Kondo exponents for two ($\alpha_{2CK} = 1$) and three ($\alpha_{3CK} = 2/5$) symmetric channels.

Crossover from quantum criticality

As the temperature is increased [up to some limit; here, $T \lesssim \min(T_K, E_C/k_B)$], the quantum critical regime is generally expected to span over a larger range of system parameters, away from the $T = 0$ quantum critical point (Fig. 5A). The so-called crossover temperature T_{co} delimits quantum criticality from below, with the critical point itself corresponding to $T_{co} = 0$. Generically, the crossover from quantum criticality as temperature is lowered should follow universal curves versus the reduced parameter T/T_{co}. Indeed, T_{co} is the only relevant temperature scale, encapsulating all microscopic details, provided that the high-energy cutoff for quantum criticality is much higher. In tunable circuits, the crossover from 2CK quantum criticality was explored versus Kondo channels asymmetry (*5*, *6*) and, in the different implementation of a spin-polarized quantum dot embedded into a dissipative circuit, versus the difference between resonant dot level and Fermi energy (*4*). These experiments corroborate the existence of a universal T/T_{co} scaling, as well as the predicted quadratic increase of T_{co} for small deviations from the 2CK critical point (*12*, *15*, *18*). We explored the disparate universal and exotic behaviors along the different crossovers induced by breaking the Kondo (pseudo)spin degeneracy or the channel symmetry, observed the development of the quantum phase transition across the symmetric 3CK quantum critical point, and demonstrated "super-ballistic" conductances.

In a first step, we investigated the so-far-unexplored crossover from 2CK and 3CK quantum criticality induced by breaking the energy degeneracy of the Kondo impurity, with the connected channels remaining symmetric. We established (i) the different 2CK and 3CK power-law dependence $T_{co} \propto |\Delta E|^\gamma$ for small energy splitting of the charge pseudospin $\Delta E = 2E_C \delta V_g/\Delta \ll E_C$, with $\Delta \simeq 0.7$ mV being the gate voltage period; (ii) a generalized expression of T_{co} for arbitrary ΔE; and (iii) the theoretical universal crossover curves $\tilde{G}_{2CK}(T/T_{co})$ and $\tilde{G}_{3CK}(T/T_{co})$, obtained analytically in (*19*, *29*) for 2CK and by NRG here for 3CK.

The crossover temperature T_{co} is defined so that the conductance is halfway between the quantum critical regime ($\approx G_{2CK}$ or $\approx G_{3CK}$, at $T_{co} \ll T \ll T_K$) and the Fermi liquid regime (≈ 0, at $T_{co} \gg T$)—that is, $G_{1,3}(\Delta E, T = T_{co}) \equiv G_{2CK}/2$ or $G_{1,2,3}(\Delta E, T = T_{co}) \equiv G_{3CK}/2$. In practice, we fixed the electronic temperature T and adjusted the energy splitting $\Delta E \propto \delta V_g$ in order to obtain this midway conductance value, if possible. In Fig. 5, B and C, this corresponds to the crossings between continuous and horizontal dashed lines, where the experimentally extracted crossover temperature directly reads $T_{co}^{expt}(\Delta E) = T$. Symbols in Fig. 5, D and E, display T_{co}^{expt} versus ΔE for the settings τ where $T_{co} \propto \Delta E^\gamma$ is expected (*32*). The predicted corresponding power laws are shown as continuous lines ($T_{co} \propto \Delta E^2$ for 2CK, $T_{co} \propto \Delta E^{5/3}$ for 3CK) (*12*). Fitting separately, for each τ, the $T_{co}^{expt}(\Delta E) \leq 12$ mK data (fulfilling the universality NRG criteria) yield the values of γ displayed as symbols in the insets of Fig. 5, D and E. A statistical analysis of these values gives $\gamma_{2CK} = 2.01 \pm 0.04$ and $\gamma_{3CK} = 1.69 \pm 0.02$ for the crossovers from 2CK and 3CK, respectively, which is in close agreement with theory.

The theoretically predicted universal crossover curves $\tilde{G}_{2CK}(T_{co}/T)$ and $\tilde{G}_{3CK}(T_{co}/T)$, shown as thick dashed lines in Fig. 5, B and C, right hand sides, are compared with conductance data. Continuous lines in Fig. 5, B and C, left hand sides represent the conductance measured at different temperatures versus gate voltage for $\tau_{1,3} \simeq 0.94$ (Fig. 5B) and $\tau_{1,2,3} \simeq 0.82$ (Fig. 5C). These settings correspond to well-developed quantum critical regimes $T \ll T_K$ (small ΔG), a necessary condition to investigate $\tilde{G}_{2CK}$ and $\tilde{G}_{3CK}$ down to small T_{co}/T. In Fig. 5, B and C, right hand sides, the gate voltage sweeps at different temperatures

Downloaded from http://science.sciencemag.org/ on September 20, 2019

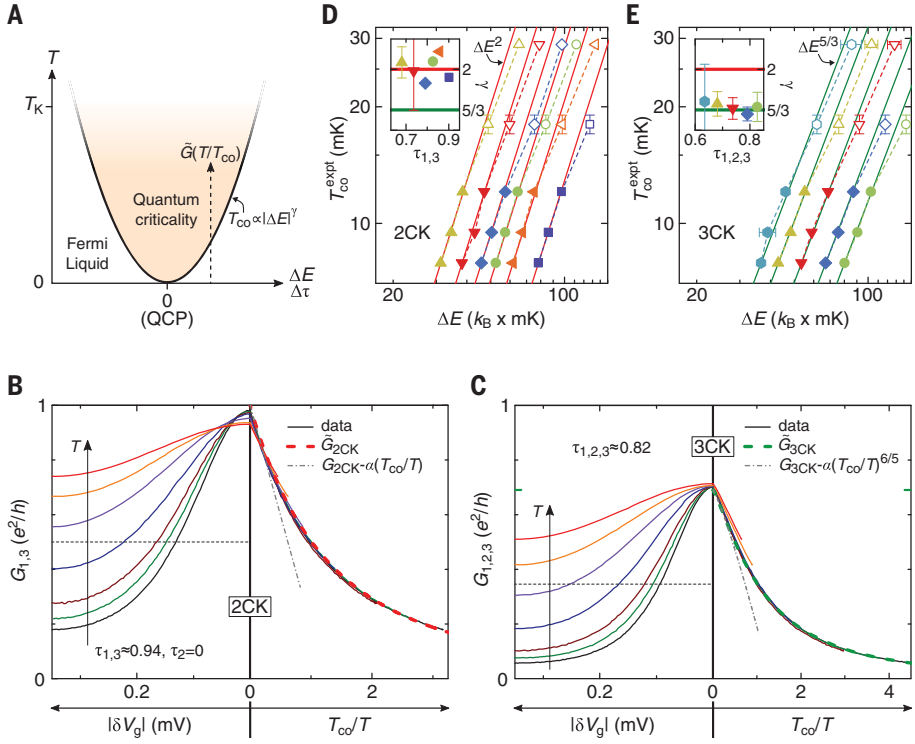

Fig. 5. Crossover from quantum criticality by pseudospin degeneracy breaking. (**A**) Quantum criticality extends as T rises. It is delimited from below by the crossover temperature T_{co}, which increases as a power law for small parameter-space distances from the critical point (for example, charge pseudospin energy splitting $\Delta E \propto \delta V_g$, channels asymmetry $\Delta\tau$). Along the crossover, theory predicts universal T/T_{co} scalings [for example, $G_i(T, \Delta E) = \tilde{G}(T/T_{co})$]. (**B** and **C**) The conductance of (B) two and (C) three symmetric channels set, respectively, to $\tau_{1,3} \simeq 0.94$ and $\tau_{1,2,3} \simeq 0.82$, are plotted as continuous lines versus $|\delta V_g|$ (left side) and T_{co}/T (right side) for $T \in \{7.9, 9.5, 12, 18, 29, 40, 55\}$ mK. Colored thick dashed lines (gray dash-dotted lines) shown in right sides display the theoretical universal crossover curves $\tilde{G}_{2CK}$ and $\tilde{G}_{3CK}$ (the predicted $T_{co}/T \ll 1$ power laws). The only fit parameter is an unknown fixed prefactor for the 3CK crossover scale T_{co} [no fit parameters in (B)]. (**D** and **E**) Experimental crossover temperatures T_{co}^{expt} are plotted as symbols in a log-log scale versus ΔE, for (D) two and (E) three symmetric channels. Each set of symbols connected by dashed lines represents one device setting $\tau_{1,3}$ or $\tau_{1,2,3}$ (insets). Full symbols correspond to $T_{co}^{expt} \leq 12$ mK. Straight continuous lines display the predicted power laws $T_{co} \propto \Delta E^{\gamma}$, with $\gamma = 2$ for 2CK and $\gamma = 5/3$ for 3CK. Fitting $T_{co}^{expt}(\Delta E) \leq 12$ mK separately for each τ yields the values of γ shown as symbols in the insets with the fit standard error.

(continuous lines) fall on top of one another when plotted versus calculated T_{co}/T, demonstrating the predicted universal character of the crossover from quantum criticality. Moreover, we found a precise match between experimental universal curves and theoretical predictions $\tilde{G}_{2CK}$ and $\tilde{G}_{3CK}$. T_{co} is obtained from experimental parameters by using generalized expressions that remain valid for arbitrary gate voltage beyond the power law at small detuning. For the charge 2CK device with near ballistic channels, the full quantitative expression derived in (*29*) was used in Fig. 5B: $T_{co} \simeq 1.444 E_C(1 - \tau_{1,3})\sin^2(\pi\delta V_g/\Delta)$. The data-$\tilde{G}_{2CK}$ comparison in Fig. 5B is therefore without any fit parameter. For 3CK, we expect from NRG calculations the similar generalization $T_{co} = \lambda_{3CK}\sin^{5/3}(\pi\delta V_g/\Delta)$ (*32*), which was used in Fig. 5C. Because the prefactor $\lambda_{3CK}(\tau, E_C)$ is not known, the value $\lambda_{3CK} = 36$ mK was freely adjusted in the data-$\tilde{G}_{3CK}$ comparison shown in Fig. 5C.

In a second step, the development of the 3CK QPT driven by the channels' competition to screen the Kondo spin is plainly observed through the conductance renormalization flow of asymmetric channels upon lowering temperature (Fig. 6). The Kondo charge pseudospin is energy degenerate ($\delta V_g = 0$), $QPC_{1,3}$ are tuned symmetric ($\tau_1 \simeq \tau_3$), and τ_2 is adjusted separately. Displayed in Fig. 6 as colored lines with arrowheads is the temperature evolution of the measured conductances G_2 (vertical axis) and $G_{1,3}$ (horizontal axis) from 55 to 7.9 mK (arrowhead at lowest T); each line corresponds to a different device setting. In total, 15 × 14 settings of $\{\tau_2, \tau_1 \simeq \tau_3\}$ were measured, with $\tau_{1,2,3}$ picked among 14 fixed values ranging from 0.1 to 0.985 (*32*) and including also $\tau_2 = 0$. The data closest to the Fig. 6 diagonal gray line correspond to three channels tuned symmetric ($\tau_1 \simeq \tau_2 \simeq \tau_3$). Below the diagonal, where $\tau_2 < \tau_1 \simeq \tau_3$, the data flow toward the predicted 2CK fixed point (Fig. 6, red disk, at $G_{1,3} = e^2/h$ and $G_2 = 0$). Above the diagonal, where $\tau_2 < \tau_1 \simeq \tau_3$ so that a flow toward the 1CK fixed point involving QPC_2 is expected (blue disk, at $G_{1,2,3} = 0$), we observed a monotonous decrease of the conductance $G_{1,3}$ across the less strongly coupled QPCs. By contrast, G_2 first rises, markedly oversteps the free-electron quantum limit e^2/h (up to +25%), and then decreases toward the zero conductance 1CK fixed point as T is further reduced.

The nonmonotonous behavior of G_2 when higher than $G_{1,3}$ might appear counterintuitive. A flow toward the low-temperature 1CK "strong coupling" fixed point is expected, which corresponds to a renormalized Kondo coupling growing monotonously ($J_2 \to \infty$). However, J_2 connects with the tunnel coupling/hopping integral of electrons across QPC_2 in the charge Kondo mapping, and free-electron theory predicts a nonmonotonous dependence of the conductance with the hopping integral [with a maximum for the value that best preserves translational invariance, and $G_2(J_2 \to \infty) = 0$]. By contrast, the present measurement of a conductance that exceeds the maximum possible value for noninteracting electrons in the ballistic limit is highly nontrivial and was not anticipated (although reproduced by our NRG calculations). Such a super-ballistic conductance, also in an intermediate temperature range and of similar amplitude, was coincidently observed in clean graphene constrictions (*37*) and explained as a collective viscous flow of the electronic fluid induced by electron-electron collisions (*38*). We speculate that the electron-electron interactions mediated by the Kondo impurity within the electronic channel across QPC_2, expected to be particularly strong near the turning point where G_2 is maximum, might also result in such a viscous electronic fluid behavior. One specificity of our system is that the super-ballistic magnitude and the temperature range in which it takes place can be controlled in situ, by separately adjusting the channels.

The experimental findings are compared with NRG calculations of the universal crossover flow from 3CK quantum criticality, induced by an initially minute asymmetry between G_2 and $G_{1,3}$ (*32*). These are displayed in Fig. 6 as two thick gray lines originating from the 3CK fixed point, with arrows pointing toward lower temperatures. For $G_{1,3} > G_2$, NRG predicts a monotonous crossover flow from 3CK to 2CK conductance fixed points that closely matches the nearby data. For $G_2 > G_{1,3}$, the universal NRG crossover flow from 3CK to 1CK reproduces the observed nonmonotonous behavior, confirms the naively expected vanishing of G_2 at the 1CK fixed point, and establishes that a super-ballistic conductance exceeding by ~20% the free-electron maximum limit follows from the 3CK model, which is in quantitative agreement with the experiment.

Downloaded from http://science.sciencemag.org/ on September 20, 2019

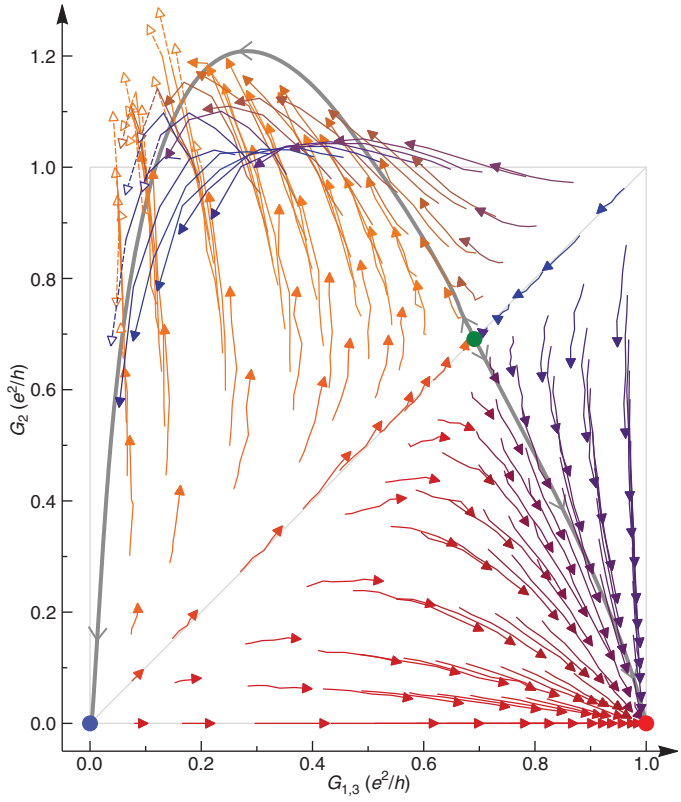

Fig. 6. Three-channel Kondo renormalization flow with super-ballistic conductances. Each colored line with an arrowhead displays the measured channels' conductance at T = 55, 40, 29, 18, 12, and 7.9 mK (arrowhead is shown at lowest T) for a fixed device tuning ($\tau_1 \approx \tau_3$, τ_2) at charge degeneracy ($\delta V_g = 0$). The lines' colors reflect the direction (the angle) of the vector connecting lowest- and highest-temperature data points, to improve readability. Because QPC_1 and QPC_3 are set symmetric [$\tau_1 \approx \tau_3$ tuned among 14 values from 0.1 to 0.985 (*32*)], only the renormalized average $G_{1,3}$ is shown on the horizontal axis. QPC_2 is separately adjusted to a coupling τ_2 selected among the same 14 values and also $\tau_2 = 0$. For the solid lines and solid arrows, the experimental standard error of G_2h/e^2 and $G_{1,3}h/e^2$ is below 0.05 (usually well below). For the dashed lines and open arrows, the standard error of G_2h/e^2 is between 0.05 and 0.1. The green, red, and blue disks correspond, respectively, to the predicted 3CK, 2CK, and 1CK low-temperature fixed points. The thick gray lines represent NRG calculations of the universal crossover flows from 3CK (*32*), with arrows pointing to lower temperatures. The conductance G_2 can markedly exceed the maximum free electron limit e^2/h.

Although experimental and NRG flows point to the same direction near 3CK and 1CK fixed points, clear crossings are also visible in intermediate regimes above the diagonal, including between different experimental device settings. These mostly take place between flows involving opposite renormalization directions of G_2, as expected from the nonmonotonous relationship between G_2 and Kondo coupling J_2 that specifically shows up above the diagonal.

Outlook

The observation of super-ballistic conductance opens a research path for low-power electronics. Although the present implementation has no clear application potential, it forms a powerful platform from which to understand the underlying mechanisms of behaviors that arise in diverse clean systems with strong electron-electron interactions. We anticipate that similar metal-semiconductor hybrids will form building blocks for a wide range of investigations of the strongly correlated electron physics, and in particular the emergence of exotic parafermion quasiparticles (*7*, *9*, *35*). Measurements of complementary observables—such as charge susceptibility, fluctuations, and heat current—as well as investigations of the dynamical and out-of-equilibrium responses could unveil yet hidden facets of the exotic underlying physics. Furthermore, direct generalizations of the present charge Kondo implementation should grant access to quantitative investigations of many thus-far-inaccessible strongly correlated phenomena (*16*, *39*), including the nanoengineered competition between Kondo channels, dissipation [specific proposal in (*40*)], fractional quantum Hall effect, and multiple impurities.

REFERENCES AND NOTES

1. S. Sachdev, *Quantum Phase Transitions* (Cambridge Univ. Press, 2011).
2. R. M. Potok, I. G. Rau, H. Shtrikman, Y. Oreg, D. Goldhaber-Gordon, *Nature* **446**, 167–171 (2007).
3. H. T. Mebrahtu *et al*., *Nature* **488**, 61–64 (2012).
4. H. Mebrahtu *et al*., *Nat. Phys.* **9**, 732–737 (2013).
5. A. J. Keller *et al*., *Nature* **526**, 237–240 (2015).
6. Z. Iftikhar *et al*., *Nature* **526**, 233–236 (2015).
7. V. J. Emery, S. Kivelson, *Phys. Rev. B Condens. Matter* **46**, 10812–10817 (1992).
8. P. Coleman, L. B. Ioffe, A. M. Tsvelik, *Phys. Rev. B Condens. Matter* **52**, 6611–6627 (1995).
9. I. Affleck, M. Oshikawa, H. Saleur, *Nucl. Phys. B* **594**, 535–606 (2001).
10. P. Nozières, A. Blandin, *J. Phys.* **41**, 193–211 (1980).
11. A. C. Hewson, *The Kondo Problem to Heavy Fermions* (Cambridge Univ. Press, 1997).
12. D. L. Cox, A. Zawadowski, *Adv. Phys.* **47**, 599–942 (1998).
13. I. Affleck, A. W. W. Ludwig, *Phys. Rev. B Condens. Matter* **48**, 7297–7321 (1993).
14. K. A. Matveev, *Phys. Rev. B Condens. Matter* **51**, 1743–1751 (1995).
15. M. Pustilnik, L. Borda, L. I. Glazman, J. von Delft, *Phys. Rev. B* **69**, 115316 (2004).
16. M. Vojta, *Philos. Mag.* **86**, 1807–1846 (2006).
17. R. Bulla, T. A. Costi, T. Pruschke, *Rev. Mod. Phys.* **80**, 395–450 (2008).
18. E. Sela, A. K. Mitchell, L. Fritz, *Phys. Rev. Lett.* **106**, 147202 (2011).
19. A. K. Mitchell, L. A. Landau, L. Fritz, E. Sela, *Phys. Rev. Lett.* **116**, 157202 (2016).
20. D. Goldhaber-Gordon *et al*., *Nature* **391**, 156–159 (1998).
21. S. M. Cronenwett, T. H. Oosterkamp, L. P. Kouwenhoven, *Science* **281**, 540–544 (1998).
22. J. Nygård, D. H. Cobden, P. E. Lindelof, *Nature* **408**, 342–346 (2000).
23. M. R. Buitelaar, A. Bachtold, T. Nussbaumer, M. Iqbal, C. Schönenberger, *Phys. Rev. Lett.* **88**, 156801 (2002).
24. L. I. Glazman, M. E. Raikh, *JETP Lett.* **47**, 452 (1988).
25. T. K. Ng, P. A. Lee, *Phys. Rev. Lett.* **61**, 1768–1771 (1988).
26. Y. Oreg, D. Goldhaber-Gordon, *Phys. Rev. Lett.* **90**, 136602 (2003).
27. S. Florens, P. Simon, S. Andergassen, D. Feinberg, *Phys. Rev. B* **75**, 155321 (2007).
28. K. A. Matveev, *Sov. Phys. JETP* **72**, 892 (1991).
29. A. Furusaki, K. A. Matveev, *Phys. Rev. B Condens. Matter* **52**, 16676–16695 (1995).
30. S. Jezouin *et al*., *Nature* **536**, 58–62 (2016).
31. E. Lebanon, A. Schiller, F. B. Anders, *Phys. Rev. B* **68**, 041311 (2003).
32. Materials and methods are available as supplementary materials.
33. Z. Iftikhar *et al*., *Nat. Commun.* **7**, 12908 (2016).
34. H. Yi, C. L. Kane, *Phys. Rev. B* **57**, R5579–R5582 (1998).
35. L. Landau, E. Cornfeld, E. Sela, Charge fractionalization in a Kondo device. *Phys. Rev. Lett.* **120**, 186801 (2018).
36. C. Kolf, J. Kroha, *Phys. Rev. B* **75**, 045129 (2007).
37. R. Krishna Kumar *et al*., *Nat. Phys.* **13**, 1182–1185 (2017).
38. H. Guo, E. Ilseven, G. Falkovich, L. S. Levitov, *Proc. Natl. Acad. Sci. U.S.A.* **114**, 3068–3073 (2017).
39. G. Kotliar, D. Vollhardt, *Phys. Today* **57**, 53–59 (2004).
40. K. Le Hur, *Phys. Rev. Lett.* **92**, 196804 (2004).

ACKNOWLEDGMENTS

We thank I. Affleck, S. Florens, L. Fritz, L. Glazman, C. Kane, K. Matveev, Y. Nazarov, E. Sela, G. Zarand, and F. Zhang for discussions. **Funding:** This work was supported by the French RENATECH network and the national French program "Investissements d'Avenir" (Labex NanoSaclay, ANR-10-LABX-0035). **Author contributions:** Z.I. and F.P. performed the experiment; Z.I., A.A., and F.P. analyzed the data; A.K.M. performed the NRG developments; C.M. and P.S. extended the analytical predictions; F.D.P. fabricated the sample with inputs from A.A.; U.G., A.C., and A.O. grew the 2DEG; and F.P. led the project and wrote the manuscript, with inputs from Z.I., A.A., A.K.M., U.G, C.M., and P.S. **Competing interests:** The authors declare no competing financial interests. **Data and materials availability:** The displayed experimental data are provided in a separate supplementary file (Data file S1). Correspondence and requests for materials should be addressed to F.P. (frederic.pierre@u-psud.fr).

SUPPLEMENTARY MATERIALS

www.sciencemag.org/content/360/6395/1315/suppl/DC1
Materials and Methods
Supplementary Text
Figs. S1 to S5
References (*41*–*52*)
Data File S1

1 May 2017; accepted 19 April 2018
Published online 3 May 2018
10.1126/science.aan5592

Downloaded from http://science.sciencemag.org/ on September 20, 2019

Science

Tunable quantum criticality and super-ballistic transport in a "charge" Kondo circuit

Z. Iftikhar, A. Anthore, A. K. Mitchell, F. D. Parmentier, U. Gennser, A. Ouerghi, A. Cavanna, C. Mora, P. Simon and F. Pierre

Science **360** (6395), 1315-1320.
DOI: 10.1126/science.aan5592originally published online May 3, 2018

A nanostructure quantum simulator

Phase transitions occurring at absolute zero temperature, or quantum phase transitions (QPTs), can be grouped into broad categories called universality classes. The classification is based on the properties of the transition rather than the microscopic details of the underlying system. Iftikhar *et al.* exploited this fact to study QPTs in clean, tunable nanostructures, rather than in complex materials, where they most often occur. Within a single nanostructure, two different classes of QPTs with profoundly different characters were studied and comprehensively characterized.

Science, this issue p. 1315

ARTICLE TOOLS http://science.sciencemag.org/content/360/6395/1315

SUPPLEMENTARY MATERIALS http://science.sciencemag.org/content/suppl/2018/05/02/science.aan5592.DC1

REFERENCES This article cites 46 articles, 3 of which you can access for free
http://science.sciencemag.org/content/360/6395/1315#BIBL

PERMISSIONS http://www.sciencemag.org/help/reprints-and-permissions

Use of this article is subject to the Terms of Service

Science (print ISSN 0036-8075; online ISSN 1095-9203) is published by the American Association for the Advancement of Science, 1200 New York Avenue NW, Washington, DC 20005. The title *Science* is a registered trademark of AAAS.

Copyright © 2018 The Authors, some rights reserved; exclusive licensee American Association for the Advancement of Science. No claim to original U.S. Government Works

Downloaded from http://science.sciencemag.org/ on September 20, 2019